Deterministic Generation of Orbital-Angular-Momentum Multiplexed Tripartite Entanglement

Sijin Li,[1,*] Xiaozhou Pan,[1,*] Yuan Ren,[1] Huanzhang Liu,[1] Sheng Yu,[1] and Jietai Jing[1,2,3,†]
[1]State Key Laboratory of Precision Spectroscopy, Joint Institute of Advanced Science and Technology, School of Physics and Electronic Science, East China Normal University, Shanghai 200062, China
[2]Department of Physics, Zhejiang University, Hangzhou 310027, China
[3]Collaborative Innovation Center of Extreme Optics, Shanxi University, Taiyuan, Shanxi 030006, China

(Received 30 October 2019; accepted 3 February 2020; published 28 February 2020)

We demonstrate the experimental generation of orbital angular momentum (OAM) multiplexed multipartite entanglement with cascaded four-wave mixing processes in a continuous variable (CV) system. In particular, we implement the simultaneous generation of 9 sets of OAM multiplexed tripartite entanglement over 27 Laguerre-Gauss (LG) modes, as well as 20 sets of OAM multiplexed bipartite entanglement over 40 LG modes, which show the rich entanglement structure of the system. In addition, we also generate tripartite entanglement of three types of coherent OAM superposition modes. Such OAM multiplexed multipartite entanglement opens the avenue to construct CV parallel quantum network for realizing parallel quantum information protocols.

DOI: 10.1103/PhysRevLett.124.083605

A quantum entangled state, originally defined in bipartite system, involves parties whose correlations are stronger than those allowed by classical physics [1]. Extending such an entangled state to a multipartite case promotes many applications in quantum information processing [2]. For example, tripartite entangled states [3], three-photon energy-time entangled states [4], and cluster states [5] are promising for constructing quantum networks [2] and realizing quantum computation [6]. In the meanwhile, multiplexing, a concept used in classical system to integrate multiple channels into a single channel provides an efficient way to enhance the channel capacity of the communication system. It is conceivable that a parallel quantum communication network and a parallel quantum computation architecture can be built if we combine the concept of multiplexing with multipartite entanglement.

Orbital angular momentum (OAM) [7], as an important physical quantity, has attracted much attention due to the advantage of a possible infinite range of OAM modes. It has been considered as an ideal degree of freedom for multiplexing to enhance data-carrying capability in classical optical communication [8,9]. Meanwhile, OAM has also been exploited in a discrete variable (DV) quantum system to generate and manipulate an OAM entangled state [10–30]. However, in sharp contrast with the wide applications of OAM in DV quantum information systems, OAM finds only a few applications in continuous variable (CV) quantum information systems, including the generation of the low-order OAM modes [31–34]. Very recently, in CV quantum systems, OAM has been applied to deterministically generate OAM multiplexed bipartite entanglement to increase the number of entanglement channels [35]. Although this work is promising, it is limited to bipartite cases. As mentioned above, multipartite entanglement is indispensable for constructing a quantum network. Therefore, in this Letter, we combine the OAM multiplexing with multipartite entanglement to demonstrate the generation of an OAM multiplexed multipartite entanglement, which is expected to be used to construct a parallel CV quantum network.

Figure 1(a) shows the detailed experimental setup for generating OAM multiplexed tripartite state from cascaded four-wave mixing (FWM) processes in two hot ^{85}Rb vapor cells. First, a strong Gaussian beam Pump_1 is injected into the Cell_1, leading to the generation of multiple pairs of Laguerre-Gauss (LG) modes: $\mathrm{LG}_{\ell,\mathrm{Pr}_1}$ and $\mathrm{LG}_{-\ell,\mathrm{Conj}_1}$ (i.e., OAM modes, ℓ is topological charge) in Pr_1 (probe) and Conj_1 (conjugate) beams, respectively. The Hamiltonian for describing the FWM process in the Cell_1 can be expressed as

$$\hat{H}_1 = i\hbar\Sigma_\ell \gamma_\ell \hat{a}^\dagger_{\ell,\mathrm{Pr}_1}\hat{b}^\dagger_{-\ell,\mathrm{Conj}_1} + \mathrm{H.c.}, \tag{1}$$

where $\hat{a}^\dagger_{\ell,\mathrm{Pr}_1}$ and $\hat{b}^\dagger_{-\ell,\mathrm{Conj}_1}$ are the creation operators associated with an OAM mode in Pr_1 and Conj_1 beams, respectively. H.c. is the Hermitian conjugate. γ_ℓ is the nonlinear interaction strength of each pair of OAM modes in this FWM process. Next in order to generate the OAM multiplexed tripartite state, the Pr_1 beam is seeded into the Cell_2 and coupled with another strong Gaussian beam Pump_2, leading to the generation of multiple pairs of $\mathrm{LG}_{\ell,\mathrm{Pr}_2}$ and $\mathrm{LG}_{-\ell,\mathrm{Conj}_2}$ modes in Pr_2 (probe) and Conj_2 (conjugate) beams, respectively. The Hamiltonian for this FWM process in the Cell_2 can be similarly expressed as

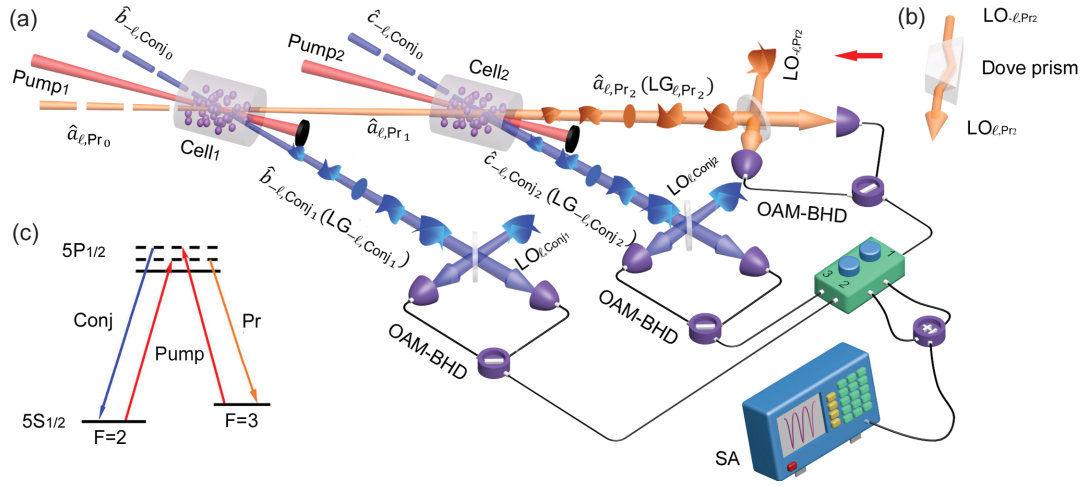

FIG. 1. (a) Experimental setup. Cell_1, Cell_2: hot ^{85}Rb vapor cells with length of 12 mm and temperature of 108 °C; Pump_1, Pump_2: the pump beams with frequency of around 377.1102 THz and waist diameter of about 900 μm. The Pump_1 and Pump_2 powers are 120 and 90 mW, respectively. The probe beam frequency is redshifted by 3.04 GHz from the pump beam. $\text{LG}_{\ell,\text{Pr}_2}$, $\text{LG}_{-\ell,\text{Conj}_1}$, and $\text{LG}_{-\ell,\text{Conj}_2}$: the LG modes in Pr_2, Conj_1, and Conj_2 beams, respectively; $\hat{a}_{\ell,\text{Pr}_2}$, $\hat{b}_{-\ell,\text{Conj}_1}$, and $\hat{c}_{-\ell,\text{Conj}_2}$: the annihilation operators of corresponding output OAM modes; $\hat{a}_{\ell,\text{Pr}_0}$ $\hat{b}_{-\ell,\text{Conj}_0}$, and $\hat{c}_{-\ell,\text{Conj}_0}$: the annihilation operators of corresponding input states; $\text{LO}_{-\ell,\text{Pr}_2}$, $\text{LO}_{\ell,\text{Conj}_1}$, and $\text{LO}_{\ell,\text{Conj}_2}$: the local oscillators; OAM-BHD: balanced homodyne detection technique for detecting OAM mode; SA: spectrum analyzer, which is set to 300 kHz resolution bandwidth, 300 Hz video bandwidth, zero span, and a center frequency of 1.5 MHz. (b) A Dove prism is inserted into the optical path of $\text{LO}_{-\ell,\text{Pr}_2}$ in order to transfer $\text{LO}_{-\ell,\text{Pr}_2}$ to $\text{LO}_{\ell,\text{Pr}_2}$. (c) Energy level diagram of the double-Λ scheme in the $D1$ line of ^{85}Rb.

$$\hat{H}_2 = i\hbar\Sigma_\ell \beta_\ell \hat{a}^\dagger_{\ell,\text{Pr}_2}\hat{c}^\dagger_{-\ell,\text{Conj}_2} + \text{H.c.}, \tag{2}$$

where $\hat{a}^\dagger_{\ell,\text{Pr}_2}$ and $\hat{c}^\dagger_{-\ell,\text{Conj}_2}$ are creation operators of corresponding OAM mode in Pr_2 and Conj_2 beams, respectively. β_ℓ is the nonlinear interaction strength of each pair of OAM modes in this FWM process. By exploiting the Heisenberg equation of motion

$$\frac{d\hat{A}}{dt} = \frac{i}{\hbar}[\hat{H}, \hat{A}], \tag{3}$$

where $\hat{A}$ is the annihilation operator of each output OAM mode, and exploiting the orthogonality of OAM modes, i.e., $[\hat{A}_\ell, \hat{A}^\dagger_{\ell'}] = \delta_{\ell,\ell'}$, the input-output relationship of OAM modes in this cascaded FWM processes can be expressed as

$$\begin{bmatrix} \hat{a}_{\ell,\text{Pr}_2} \\ \hat{b}^\dagger_{-\ell,\text{Conj}_1} \\ \hat{c}^\dagger_{-\ell,\text{Conj}_2} \end{bmatrix} = \begin{bmatrix} \sqrt{G_{\ell,1}G_{\ell,2}} & \sqrt{G_{\ell,2}g_{\ell,1}} & \sqrt{g_{\ell,2}} \\ \sqrt{g_{\ell,1}} & \sqrt{G_{\ell,1}} & 0 \\ \sqrt{G_{\ell,1}g_{\ell,2}} & \sqrt{g_{\ell,1}g_{\ell,2}} & \sqrt{G_{\ell,2}} \end{bmatrix} \begin{bmatrix} \hat{a}_{\ell,\text{Pr}_0} \\ \hat{b}^\dagger_{-\ell,\text{Conj}_0} \\ \hat{c}^\dagger_{-\ell,\text{Conj}_0} \end{bmatrix}, \tag{4}$$

where $\hat{a}_{\ell,\text{Pr}_0}$ ($\hat{b}^\dagger_{-\ell,\text{Conj}_0}$, $\hat{c}^\dagger_{-\ell,\text{Conj}_0}$) is the annihilation (creation) operator of the corresponding input state, $G_{\ell,1} = \cosh^2(\gamma_\ell t_1)$ and $G_{\ell,2} = \cosh^2(\beta_\ell t_2)$ are the intensity gains of OAM modes in these two FWM processes, respectively, t_1 and t_2 are the mixing interaction time, $G_{\ell,1} - g_{\ell,1} = 1$, $G_{\ell,2} - g_{\ell,2} = 1$. Consequently, multiple sets of $\text{LG}_{\ell,\text{Pr}_2}$, $\text{LG}_{-\ell,\text{Conj}_1}$ and $\text{LG}_{-\ell,\text{Conj}_2}$ modes form the OAM multiplexed tripartite state.

To witness the entanglement of such OAM multiplexed tripartite state, we need to derive the covariance matrix (CM), which can be used to fully characterize the quantum properties of Gaussian states. The CM is composed of covariances of phase and amplitude quadratures, i.e., $\sigma = \langle \xi\xi^T \rangle$, where σ is CM, $\hat{\xi} = (\hat{X}_{\hat{a}_{\ell,\text{Pr}_2}}, \hat{Y}_{\hat{a}_{\ell,\text{Pr}_2}}, \hat{X}_{\hat{b}_{-\ell,\text{Conj}_1}}, \hat{Y}_{\hat{b}_{-\ell,\text{Conj}_1}}, \hat{X}_{\hat{c}_{-\ell,\text{Conj}_2}}, \hat{Y}_{\hat{c}_{-\ell,\text{Conj}_2}})^T$, and $\hat{X} = \hat{A} + \hat{A}^\dagger$, $\hat{Y} = i(\hat{A}^\dagger - \hat{A})$ stand for the amplitude and phase quadratures of each output OAM mode, respectively. Then we test the entanglement of each set of $\text{LG}_{\ell,\text{Pr}_2}$, $\text{LG}_{-\ell,\text{Conj}_1}$ and $\text{LG}_{-\ell,\text{Conj}_2}$ modes by using the positivity under partial transposition (PPT) criterion [36]. The entanglement of the OAM tripartite state can be testified by three possible 1×2 partitions, which are $\text{LG}_{-\ell,\text{Conj}_1}|(\text{LG}_{\ell,\text{Pr}_2}, \text{LG}_{-\ell,\text{Conj}_2})$, $\text{LG}_{\ell,\text{Pr}_2}|(\text{LG}_{-\ell,\text{Conj}_1}, \text{LG}_{-\ell,\text{Conj}_2})$, and $\text{LG}_{-\ell,\text{Conj}_2}|(\text{LG}_{\ell,\text{Pr}_2}, \text{LG}_{\ell,\text{Conj}_1})$. Based on these partitions, the smallest

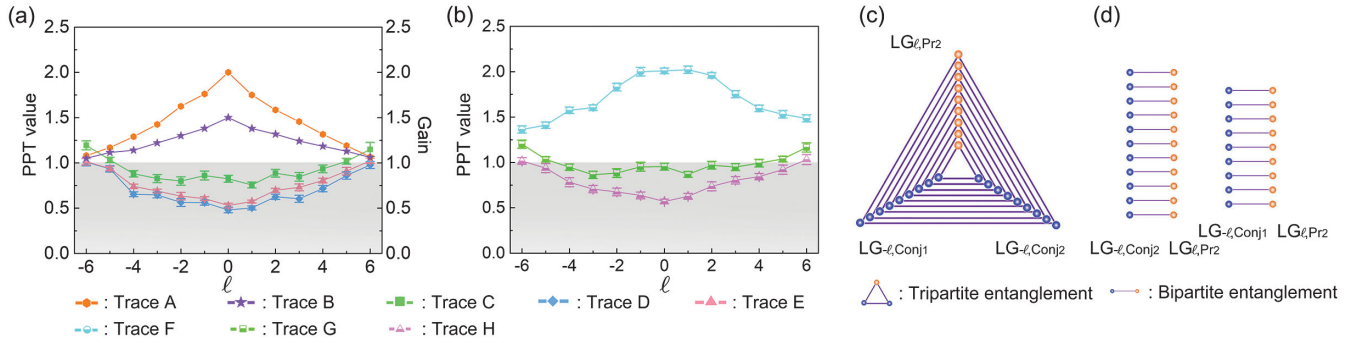

FIG. 2. Witnessing an OAM multiplexed tripartite and bipartite entanglement. (a) The test of tripartite entanglement among $\mathrm{LG}_{\ell,\mathrm{Pr}_2}$, $\mathrm{LG}_{-\ell,\mathrm{Conj}_1}$, and $\mathrm{LG}_{-\ell,\mathrm{Conj}_2}$ modes. Traces A and B correspond to two intensity gains $G_{\ell,1}$ and $G_{\ell,2}$, respectively. Traces C, D, and E correspond to three PPT values of $\mathrm{LG}_{-\ell,\mathrm{Conj}_1}|(\mathrm{LG}_{\ell,\mathrm{Pr}_2},\mathrm{LG}_{-\ell,\mathrm{Conj}_2})$, $\mathrm{LG}_{\ell,\mathrm{Pr}_2}|(\mathrm{LG}_{-\ell,\mathrm{Conj}_1},\mathrm{LG}_{-\ell,\mathrm{Conj}_2})$, and $\mathrm{LG}_{-\ell,\mathrm{Conj}_2}|(\mathrm{LG}_{\ell,\mathrm{Pr}_2},\mathrm{LG}_{-\ell,\mathrm{Conj}_1})$ partitions, respectively. (b) The test of bipartite entanglement between any two of the three LG modes $\mathrm{LG}_{\ell,\mathrm{Pr}_2}$, $\mathrm{LG}_{-\ell,\mathrm{Conj}_1}$, and $\mathrm{LG}_{-\ell,\mathrm{Conj}_2}$. Traces F, G, and H correspond to three PPT values of $\mathrm{LG}_{-\ell,\mathrm{Conj}_1}|\mathrm{LG}_{-\ell,\mathrm{Conj}_2}$, $\mathrm{LG}_{\ell,\mathrm{Pr}_2}|\mathrm{LG}_{-\ell,\mathrm{Conj}_1}$, and $\mathrm{LG}_{\ell,\mathrm{Pr}_2}|\mathrm{LG}_{-\ell,\mathrm{Conj}_2}$ partitions, respectively. Error bars of PPT values are present as data deviations. (c) Diagram of OAM multiplexed tripartite entanglement. (d) Diagram of OAM multiplexed bipartite entanglement.

symplectic eigenvalue of the partially transposed CM, i.e., the PPT value, is obtained by calculating the absolute eigenvalue of $iJ\tilde{\sigma}_k$, where $\tilde{\sigma}_k = T_k \sigma T_k^T$, T_k is a 6×6 diagonal matrix with all diagonal elements equal to 1 except for $T_{2k,2k} = -1$ ($k = 1$, 2, and 3), and $J = \bigoplus_{k=1}^{3} \left(\begin{smallmatrix} 0 & 1 \\ -1 & 0 \end{smallmatrix}\right)$ is the symplectic transformation matrix. If all the PPT values of the three possible partitions are smaller than 1, then genuine tripartite entanglement is generated.

Experimentally we obtain CM by using three sets of balanced homodyne detection (BHD) systems to detect OAM modes [35]. In this BHD technique, the LG mode with topological charge ℓ can only be extracted by a local oscillator (LO) of LG mode with topological charge $-\ell$. Thus we use a spatial light modulator (SLM), which loads a computer-generated hologram to generate a bright LG beam. Then we set up a set of new cascaded FWM processes seeded by this bright LG beam to generate three LO beams $\mathrm{LO}_{-\ell,\mathrm{Pr}_2}$, $\mathrm{LO}_{\ell,\mathrm{Conj}_1}$, and $\mathrm{LO}_{\ell,\mathrm{Conj}_2}$, which can be used to extract three OAM modes: $\mathrm{LG}_{\ell,\mathrm{Pr}_2}$, $\mathrm{LG}_{-\ell,\mathrm{Conj}_1}$, and $\mathrm{LG}_{-\ell,\mathrm{Conj}_2}$, respectively. Each element of CM can be experimentally obtained by

$$\langle \hat{Q}_i \hat{Q}_j \rangle = \frac{\pm\Delta^2 \hat{Q}_{\pm,i,j} \mp \Delta^2(L_i \hat{Q}_i) \mp \Delta^2(L_j \hat{Q}_j)}{2\sqrt{\Delta^2(L_i \hat{Q}_{\mathrm{vac}})}\sqrt{\Delta^2(L_j \hat{Q}_{\mathrm{vac}})}}, \quad (5)$$

where $\hat{Q}_i$ ($\hat{Q}_j$) is $\hat{X}$ or $\hat{Y}$ quadrature, i and j denote the three output OAM modes, "vac" denotes a vacuum mode, $\Delta^2 \hat{Q}_{\pm,i,j} = \Delta^2(L_i \hat{Q}_i \pm L_j \hat{Q}_j)$ is measured by combining two BHDs via an adder or subtractor, L_i^2 (L_j^2) is LO beam intensity, $\Delta^2(L_i \hat{Q}_i)$ [$\Delta^2(L_j \hat{Q}_j)$] is measured by the single BHD, $\Delta^2(L_i \hat{Q}_{\mathrm{vac}})$ [$\Delta^2(L_j \hat{Q}_{\mathrm{vac}})$] is measured by blocking the signal beam of the corresponding BHD. After obtaining CM, the PPT values can be calculated to testify the entanglement of each set of OAM multiplexed tripartite state.

Figure 2(a) shows the results of PPT values as functions of ℓ (see the Supplemental Material for images of output fields [37]). We find that the larger the $|\ell|$ is, the lower the intensity gains $G_{\ell,1}$ and $G_{\ell,2}$ will be, as shown in traces A and B, respectively. This is due to the beam size increase of the OAM modes with the increase of the $|\ell|$. Such beam size increase will reduce the overlap of OAM modes with the pump beams and thus reduce their nonlinear interaction strength. In addition, it can be seen that for ℓ in the range of -4 to 4, the three PPT values (traces C, D, and E) for the case of each ℓ are all smaller than 1 (within the gray region), which demonstrates the generation of 9 sets of OAM multiplexed tripartite entanglement, as depicted in Fig. 2(c). Some of the three PPT values are larger than 1 when $|\ell|$ is increased to 5 and 6, showing the disappearance of genuine tripartite entanglement. This is actually due to the disappearance of the nonlinear interaction strength for the case of large $|\ell|$, which defines the OAM bandwidth [35,40] of tripartite entanglement in this system. Meanwhile, it is also interesting to investigate the bipartite entanglement between any two of the three generated LG modes. The corresponding results of PPT values are shown in Fig. 2(b). It can be seen that the PPT values of $\mathrm{LG}_{\ell,\mathrm{Pr}_2}|\mathrm{LG}_{-\ell,\mathrm{Conj}_1}$ partition (trace G, ℓ from -4 to 4) and the PPT values of $\mathrm{LG}_{\ell,\mathrm{Pr}_2}|\mathrm{LG}_{-\ell,\mathrm{Conj}_2}$ partition (trace H, ℓ from -5 to 5) are all smaller than 1, clearly showing that the $\mathrm{LG}_{\ell,\mathrm{Pr}_2}$ mode is entangled with both $\mathrm{LG}_{-\ell,\mathrm{Conj}_1}$ and $\mathrm{LG}_{-\ell,\mathrm{Conj}_2}$ modes. It is also clear that the $\mathrm{LG}_{-\ell,\mathrm{Conj}_1}$ and $\mathrm{LG}_{-\ell,\mathrm{Conj}_2}$ modes are not entangled since the PPT values of $\mathrm{LG}_{-\ell,\mathrm{Conj}_1}|\mathrm{LG}_{-\ell,\mathrm{Conj}_2}$ partition (trace F) are always larger than 1 for ℓ ranging from -6 to 6. This is due to the fact that the $\mathrm{LG}_{-\ell,\mathrm{Conj}_1}$ and $\mathrm{LG}_{-\ell,\mathrm{Conj}_2}$ modes have never interacted with each other directly. The presence of tripartite and

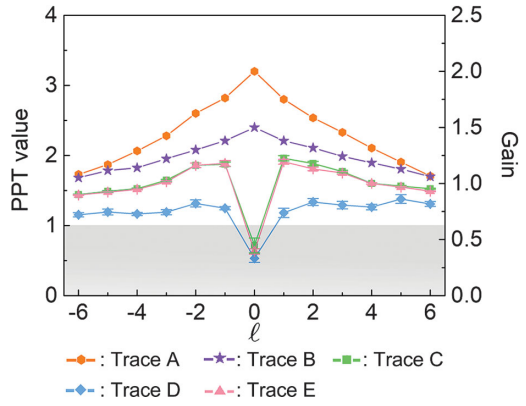

FIG. 3. Testing the OAM multiplexed tripartite entanglement among $\mathrm{LG}_{-\ell,\mathrm{Pr}_2}$, $\mathrm{LG}_{-\ell,\mathrm{Conj}_1}$, and $\mathrm{LG}_{-\ell,\mathrm{Conj}_2}$ modes. Traces A and B correspond to two intensity gains $G_{\ell,1}$ and $G_{\ell,2}$, respectively. Traces C, D, and E correspond to three PPT values of $\mathrm{LG}_{-\ell,\mathrm{Conj}_1}|(\mathrm{LG}_{-\ell,\mathrm{Pr}_2},\mathrm{LG}_{-\ell,\mathrm{Conj}_2})$, $\mathrm{LG}_{-\ell,\mathrm{Pr}_2}|(\mathrm{LG}_{-\ell,\mathrm{Conj}_1},\mathrm{LG}_{-\ell,\mathrm{Conj}_2})$, and $\mathrm{LG}_{-\ell,\mathrm{Conj}_2}|(\mathrm{LG}_{-\ell,\mathrm{Pr}_2},\mathrm{LG}_{-\ell,\mathrm{Conj}_1})$ partitions, respectively. Error bars of PPT values are present as data deviations.

bipartite entanglement shows the rich entanglement structure of the system. In other words, this cascaded FWM system can provide 9 sets of OAM multiplexed tripartite entanglement of $\mathrm{LG}_{\ell,\mathrm{Pr}_2}$, $\mathrm{LG}_{-\ell,\mathrm{Conj}_1}$, and $\mathrm{LG}_{-\ell,\mathrm{Conj}_2}$ modes as depicted in Fig. 2(c), as well as 9 (11) sets of OAM multiplexed bipartite entanglement between $\mathrm{LG}_{\ell,\mathrm{Pr}_2}$ and $\mathrm{LG}_{-\ell,\mathrm{Conj}_1}$ ($\mathrm{LG}_{-\ell,\mathrm{Conj}_2}$) modes as depicted in Fig. 2(d). Besides, these experimental results also show that these entangled OAM modes are generated in pairs in each FWM process, which clearly confirms the OAM conservation in the FWM process [35].

To illustrate the decisive role of OAM conservation in preparing the above mentioned OAM multiplexed tripartite entanglement, we test the quantum entanglement among the LG modes: $\mathrm{LG}_{-\ell,\mathrm{Pr}_2}$, $\mathrm{LG}_{-\ell,\mathrm{Conj}_1}$, and $\mathrm{LG}_{-\ell,\mathrm{Conj}_2}$. To this end, the three local oscillator (LO) beams $\mathrm{LO}_{\ell,\mathrm{Pr}_2}$, $\mathrm{LO}_{\ell,\mathrm{Conj}_1}$, and $\mathrm{LO}_{\ell,\mathrm{Conj}_2}$ are required. Thus a Dove prism is inserted in the light path of $\mathrm{LO}_{-\ell,\mathrm{Pr}_2}$ to transfer it to $\mathrm{LO}_{\ell,\mathrm{Pr}_2}$, as shown in Fig. 1(b). The corresponding results of PPT values are shown in Fig. 3. It can be seen that the three PPT values (traces C, D, and E) for any nonzero ℓ are all larger than 1 (above the gray region), demonstrating no genuine tripartite entanglement among $\mathrm{LG}_{-\ell,\mathrm{Pr}_2}$, $\mathrm{LG}_{-\ell,\mathrm{Conj}_1}$, and $\mathrm{LG}_{-\ell,\mathrm{Conj}_2}$ ($\ell \neq 0$) modes. Moreover, the higher the intensity gains $G_{\ell,1}$ and $G_{\ell,2}$ (traces A and B) are, the larger the PPT values will be, which shows the stronger uncorrelated noises shared among these LG modes. For the case of $\ell = 0$, the three PPT values are all smaller than 1, demonstrating the generation of genuine tripartite entanglement of three Gaussian modes, which is consistent with the corresponding result in Fig. 2(a). Thus, it can be concluded that OAM multiplexed tripartite entanglement is only distributed among specific OAM modes, which are determined by the OAM conservation of FWM process.

So far, we have studied the tripartite entanglement of OAM modes carrying single topological charge. It is also

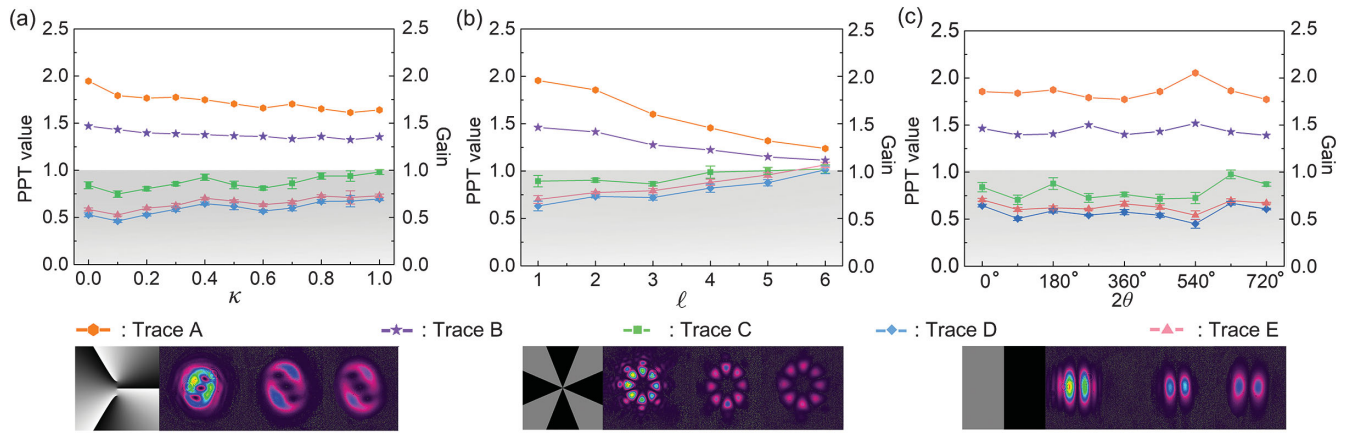

FIG. 4. Witnessing the tripartite entanglement for three types of coherent OAM superposition modes. For all subfigures, traces A and B correspond to two intensity gains G_1 and G_2 of two FWM processes, respectively. Traces C, D, and E correspond to three PPT values of $\mathrm{Conj}_1|(\mathrm{Pr}_2,\mathrm{Conj}_2)$, $\mathrm{Pr}_2|(\mathrm{Conj}_1,\mathrm{Conj}_2)$, and $\mathrm{Conj}_2|(\mathrm{Pr}_2,\mathrm{Conj}_1)$ partitions, respectively. (a) The test of tripartite entanglement among $\sqrt{\kappa}\mathrm{LG}_{3,\mathrm{Pr}_2}+\sqrt{1-\kappa}\mathrm{LG}_{1,\mathrm{Pr}_2}$, $\sqrt{\kappa}\mathrm{LG}_{-3,\mathrm{Conj}_1}+\sqrt{1-\kappa}\,\mathrm{LG}_{-1,\mathrm{Conj}_1}$, and $\sqrt{\kappa}\mathrm{LG}_{-3,\mathrm{Conj}_2}+\sqrt{1-\kappa}\,\mathrm{LG}_{-1,\mathrm{Conj}_2}$ modes by varying κ. The second row shows the computer-generated hologram and the images of Pr_2, Conj_1, and Conj_2 beams with corresponding OAM superposition modes in the case of $\kappa = 0.5$, respectively. (b) The test of tripartite entanglement among $\mathrm{LG}_{\ell,\mathrm{Pr}_2}+\mathrm{LG}_{-\ell,\mathrm{Pr}_2}$, $\mathrm{LG}_{-\ell,\mathrm{Conj}_1}+\mathrm{LG}_{\ell,\mathrm{Conj}_1}$, and $\mathrm{LG}_{-\ell,\mathrm{Conj}_2}+\mathrm{LG}_{\ell,\mathrm{Conj}_2}$ modes by varying ℓ. The second row shows the computer-generated hologram and the images of Pr_2, Conj_1, and Conj_2 beams with corresponding OAM superposition modes in the case of $\ell = 4$, respectively. (c) The test of tripartite entanglement among $\mathrm{LG}_{1,\mathrm{Pr}_2}+e^{2i\theta}\mathrm{LG}_{-1,\mathrm{Pr}_2}$, $\mathrm{LG}_{-1,\mathrm{Conj}_1}+e^{2i\theta}\mathrm{LG}_{1,\mathrm{Conj}_1}$, and $\mathrm{LG}_{-1,\mathrm{Conj}_2}+e^{2i\theta}\mathrm{LG}_{1,\mathrm{Conj}_2}$ modes by varying relative phase 2θ. The second row shows the computer-generated hologram and the images of Pr_2, Conj_1, and Conj_2 beams with corresponding OAM superposition modes in the case of $2\theta = 360°$, respectively. Error bars of PPT values are present as data deviations.

interesting to study the tripartite entanglement of coherent OAM superposition modes [10]. Thus a more complicated hologram is loaded onto the SLM to generate the appropriate LO beams. The corresponding results are shown in Fig. 4, where traces A and B correspond to intensity gains G_1 and G_2, respectively, traces C, D, and E correspond to three PPT values. Figure 4(a) shows that the three PPT values are all smaller than 1, which demonstrates the genuine tripartite entanglement among $\sqrt{\kappa}\mathrm{LG}_{3,\mathrm{Pr}_2}+\sqrt{1-\kappa}\mathrm{LG}_{1,\mathrm{Pr}_2}$, $\sqrt{\kappa}\mathrm{LG}_{-3,\mathrm{Conj}_1}+\sqrt{1-\kappa}\mathrm{LG}_{-1,\mathrm{Conj}_1}$, and $\sqrt{\kappa}\mathrm{LG}_{-3,\mathrm{Conj}_2}+\sqrt{1-\kappa}\mathrm{LG}_{-1,\mathrm{Conj}_2}$ modes for any κ within the range of [0, 1]. Figure 4(b) shows that the three PPT values are smaller than 1 for ℓ in a range of 1 to 4, which demonstrates the genuine tripartite entanglement among $\mathrm{LG}_{\ell,\mathrm{Pr}_2}+\mathrm{LG}_{-\ell,\mathrm{Pr}_2}$, $\mathrm{LG}_{-\ell,\mathrm{Conj}_1}+\mathrm{LG}_{\ell,\mathrm{Conj}_1}$, and $\mathrm{LG}_{-\ell,\mathrm{Conj}_2}+\mathrm{LG}_{\ell,\mathrm{Conj}_2}$ modes. For $\ell=5$, 6, some of the three PPT values are larger than 1, which shows the disappearance of the genuine tripartite entanglement for this type of coherent OAM superposition mode. Figure 4(c) shows that the three PPT values are all smaller than 1, which demonstrates the genuine tripartite entanglement among $\mathrm{LG}_{1,\mathrm{Pr}_2}+e^{2i\theta}\mathrm{LG}_{-1,\mathrm{Pr}_2}$, $\mathrm{LG}_{-1,\mathrm{Conj}_1}+e^{2i\theta}\mathrm{LG}_{1,\mathrm{Conj}_1}$, and $\mathrm{LG}_{-1,\mathrm{Conj}_2}+e^{2i\theta}\mathrm{LG}_{1,\mathrm{Conj}_2}$ modes.

In conclusion, we have experimentally demonstrated the generation of 9 sets of OAM multiplexed tripartite entanglement as well as 20 sets of OAM multiplexed bipartite entanglement in CV regime by exploiting cascaded FWM processes. In addition, we have also experimentally shown that there is no tripartite entanglement among $\mathrm{LG}_{-\ell,\mathrm{Pr}_2}$, $\mathrm{LG}_{-\ell,\mathrm{Conj}_1}$, and $\mathrm{LG}_{-\ell,\mathrm{Conj}_2}$ modes, which verifies the importance of the OAM conservation for generating OAM multiplexed tripartite entanglement in this system. Furthermore, we have investigated the tripartite entanglement for three types of coherent OAM superposition modes. As far as we know, the experimental generation of multipartite entanglement from cascaded FWM processes has not been reported. Although the multiple quantum correlated beams have been generated from such a system in our previous work [41], it only focuses on intensity correlation and is far from the demonstration of multipartite entanglement, which requires the measurement of both amplitude and phase quadratures. Such OAM multiplexed multipartite entanglement can be used to construct a parallel CV multichannel quantum network. In such a parallel quantum network, each set of multipartite entanglement can be distributed to each channel to realize various different quantum information tasks, such as quantum state sharing [42], quantum teleportation network [43], and controlled dense coding [44]. Thus, the channel capacity and diversity of the quantum network can be greatly enhanced. Our work opens the avenue for realizing the parallel quantum information protocols.

This work was funded by the National Natural Science Foundation of China (NSFC) (Grants No. 11874155, No. 91436211, No. 11374104, and No. 10974057), the Natural Science Foundation of Shanghai (Grant No. 17ZR1442900), the Minhang Leading Talents (Grant No. 201971), the Program of Scientific and Technological Innovation of Shanghai (Grant No. 17JC1400401), the National Basic Research Program of China (Grant No. 2016YFA0302103), the 111 project (Grant No. B12024), and the Fundamental Research Funds for the Central Universities.

*These authors contributed equally to this work.
†jtjing@phy.ecnu.edu.cn

[1] A. Einstein, B. Podolsky, and N. Rosen, Phys. Rev. **47**, 777 (1935).
[2] S. L. Braunstein and P. van Loock, Rev. Mod. Phys. **77**, 513 (2005).
[3] H. Yonezawa, T. Aoki, and A. Furusawa, Nature (London) **431**, 430 (2004).
[4] L. K. Shalm, D. R. Hamel, Z. Yan, C. Simon, K. J. Resch, and T. Jennewein, Nat. Phys. **9**, 19 (2013).
[5] Y. Cai, J. Roslund, G. Ferrini, F. Arzani, X. Xu, C. Fabre, and N. Treps, Nat. Commun. **8**, 15645 (2017).
[6] C. Weedbrook, S. Pirandola, R. García-Patrón, N. J. Cerf, T. C. Ralph, J. H. Shapiro, and S. Lloyd, Rev. Mod. Phys. **84**, 621 (2012).
[7] L. Allen, M. W. Beijersbergen, R. J. C. Spreeuw, and J. P. Woerdman, Phys. Rev. A **45**, 8185 (1992).
[8] J. Wang, J. Yang, I. M. Fazal, N. Ahmed, Y. Yan, H. Huang, Y. Ren, Y. Yue, S. Dolinar, M. Tur, and A. E. Willner, Nat. Photonics **6**, 488 (2012).
[9] N. Bozinovic, Y. Yue, Y. Ren, M. Tur, P. Kristensen, H. Huang, A. E. Willner, and S. Ramachandran, Science **340**, 1545 (2013).
[10] R. Fickler, R. Lapkiewicz, W. N. Plick, M. Krenn, C. Schaeff, S. Ramelow, and A. Zeilinger, Science **338**, 640 (2012).
[11] A. Mair, A. Vaziri, G. Weihs, and A. Zeilinger, Nature (London) **412**, 313 (2001).
[12] A. C. Dada, J. Leach, G. S. Buller, M. J. Padgett, and E. Andersson, Nat. Phys. **7**, 677 (2011).
[13] M. Malik, M. Erhard, M. Huber, M. Krenn, R. Fickler, and A. Zeilinger, Nat. Photonics **10**, 248 (2016).
[14] J.-C. Lee, K.-K. Park, T.-M. Zhao, and Y.-H. Kim, Phys. Rev. Lett. **117**, 250501 (2016).
[15] T.-M. Zhao, Y. S. Ihn, and Y.-H. Kim, Phys. Rev. Lett. **122**, 123607 (2019).
[16] Z.-Q. Zhou, Y.-L. Hua, X. Liu, G. Chen, J.-S. Xu, Y.-J. Han, C.-F. Li, and G.-C. Guo, Phys. Rev. Lett. **115**, 070502 (2015).
[17] M. Mafu, A. Dudley, S. Goyal, D. Giovannini, M. McLaren, M. J. Padgett, T. Konrad, F. Petruccione, N. Lütkenhaus, and A. Forbes, Phys. Rev. A **88**, 032305 (2013).
[18] A. Sit, F. Bouchard, R. Fickler, J. Gagnon-Bischoff, H. Larocque, K. Heshami, D. Elser, C. Peuntinger, K. Günthner, B. Heim, C. Marquardt, G. Leuchs, R. W. Boyd, and E. Karimi, Optica **4**, 1006 (2017).
[19] X.-L. Wang, X.-D. Cai, Z.-E. Su, M.-C.Chen, D. Wu, L. Li, N.-L. Liu, C.-Y. Lu, and J.-W. Pan, Nature (London) **518**, 516 (2015).

[20] W. Zhang, D.-S. Ding, M.-X. Dong, S. Shi, K. Wang, S.-L. Liu, Y. Li, Z.-Y. Zhou, B.-S. Shi, and G.-C. Guo, Nat. Commun. **7**, 13514 (2016).
[21] Y. Zhang, M. Agnew, T. Roger, F. S. Roux, T. Konrad, D. Faccio, J. Leach, and A. Forbes, Nat. Commun. **8**, 632 (2017).
[22] A. Vaziri, G. Weihs, and A. Zeilinger, Phys. Rev. Lett. **89**, 240401 (2002).
[23] S. S. R. Oemrawsingh, X. Ma, D. Voigt, A. Aiello, E. R. Eliel, G. W.'t Hooft, and J. P. Woerdman, Phys. Rev. Lett. **95**, 240501 (2005).
[24] G. Molina-Terriza, J. P. Torres, and L. Torner, Nat. Phys. **3**, 305 (2007).
[25] J. Leach, B. Jack, J. Romero, A. K. Jha, A. M. Yao, S. Franke-Arnold, D. G. Ireland, R. W. Boyd, S. M. Barnett, and M. J. Padgett, Science **329**, 662 (2010).
[26] F. Bouchard, R. Fickler, R. W. Boyd, and E. Karimi, Sci. Adv. **3**, e1601915 (2017).
[27] D.-S. Ding, W. Zhang, Z.-Y. Zhou, S. Shi, G.-Y. Xiang, X.-S. Wang, Y.-K. Jiang, B.-S. Shi, and G.-C. Guo, Phys. Rev. Lett. **114**, 050502 (2015).
[28] Z.-Y. Zhou, S.-L. Liu, Y. Li, D.-S. Ding, W. Zhang, S. Shi, M.-X. Dong, B.-S. Shi, and G.-C. Guo, Phys. Rev. Lett. **117**, 103601 (2016).
[29] B. C. Hiesmayr, M. J. A. de Dood, and W. Löffler, Phys. Rev. Lett. **116**, 073601 (2016).
[30] X.-L. Wang, Y.-H. Luo, H.-L. Huang, M.-C. Chen, Z.-E. Su, C. Liu, C. Chen, W. Li, Y.-Q. Fang, X. Jiang, J. Zhang, L. Li, N.-L. Liu, C.-Y. Lu, and J.-W. Pan, Phys. Rev. Lett. **120**, 260502 (2018).
[31] M. Lassen, G. Leuchs, and U. L. Andersen, Phys. Rev. Lett. **102**, 163602 (2009).
[32] K. Liu, J. Guo, C. Cai, S. Guo, and J. Gao, Phys. Rev. Lett. **113**, 170501 (2014).
[33] A. M. Marino, V. Boyer, R. C. Pooser, P. D. Lett, K. Lemons, and K. M. Jones, Phys. Rev. Lett. **101**, 093602 (2008).
[34] V. Boyer, A. M. Marino, and P. D. Lett, Phys. Rev. Lett. **100**, 143601 (2008).
[35] X. Pan, S. Yu, Y. Zhou, K. Zhang, K. Zhang, S. Lv, S. Li, W. Wang, and J. Jing, Phys. Rev. Lett. **123**, 070506 (2019).
[36] R. Simon, Phys. Rev. Lett. **84**, 2726 (2000).
[37] See the Supplemental Material at http://link.aps.org/supplemental/10.1103/PhysRevLett.124.083605 for images of output fields and the verification of topological charges of output OAM modes, which includes Refs. [38,39].
[38] A. Ya. Bekshaev, M. S. Soskin, and M. V. Vasnetsov, J. Opt. Soc. Am. A **20**, 1635 (2003).
[39] P. Vaity, J. Banerji, and R. P. Singh, Phys. Lett. A **377**, 1154 (2013).
[40] R. F. Offer, D. Stulga, E. Riis, S. Franke-Arnold, and A. S. Arnold, Commun. Phys. **1**, 84 (2018).
[41] Z. Qin, L. Cao, H. Wang, A. M. Marino, W. Zhang, and J. Jing, Phys. Rev. Lett. **113**, 023602 (2014).
[42] A. M. Lance, T. Symul, W. P. Bowen, B. C. Sanders, and P. K. Lam, Phys. Rev. Lett. **92**, 177903 (2004).
[43] H. Yonezawa, T. Aoki, and A. Furusawa, Nature (London) **431**, 430 (2004).
[44] J. Jing, J. Zhang, Y. Yan, F. Zhao, C. Xie, and K. Peng, Phys. Rev. Lett. **90**, 167903 (2003).